Rare Metal Materials and Engineering
Volume 47, Issue 11, November 2018
Online English edition of the Chinese language journal

Cite this article as: Rare Metal Materials and Engineering, 2018, 47(11): 3329-3337.

ARTICLE

Prediction of Flow Stresses for a Typical Nickel-Based Superalloy During Hot Deformation Based on Dynamic Recrystallization Kinetic Equation

Zhou Haiping[1], Zhang Hongbin[1], Liu Jie[1], Qin Shengxue[1,2], Lv Yuting[1]

[1] Shandong University of Science and Technology, Qingdao 266590, China; [2] Qingdao RTP Engineering Technology Center, Qingdao 266590, China

Abstract: The hot deformation behavior of a typical nickel-based superalloy was investigated by isothermal compression tests in the temperature range of 1010~1160 ºC and strain rate range of 0.001~1 s^{-1}. The results indicate that the work hardening, dynamic recovery (DRV) and dynamic recrystallization (DRX) occurred in the alloy during hot deformation. Considering the coupled effects of deformation parameters on the flow behaviors of the alloy, the constitutive models were established to predict the flow stresses during the work hardening-DRV period and DRX periods. In the DRX period, the modified DRX kinetic equation was used to develop the constitutive models, and the strain for maximum softening rate was used in this equation. Additionally, the material constants in the constitutive models were expressed as the functions of Zener-Hollomon parameter by using a linear fitting method. Meanwhile, comparisons between the measured and the predicted flow stresses were carried out, while the correlation coefficient (R) and average absolute relative error (AARE) between the measured and predicted values were also calculated. The results confirm that the developed models could give an accurate estimation of the flow stresses.

Key words: nickel-based superalloy; constitutive model; work hardening; DRV; DRX

During hot deformation, the flow behaviors of metals and alloys are very complex, and the control of microstructure is very important for optimizing the final mechanical properties of the products[1-3]. Meanwhile, it is well known that the work hardening, dynamic recovery (DRV) and dynamic recrystallization (DRX)[4,5] often occur in the metals and alloys during hot deformation, resulting in the complex flow behaviors. Moreover, both the working hardening and dynamic softening mechanisms are significantly affected by the deformation parameters, such as deformation temperature, strain rate and strain[6]. In other words, a given combination of deformation parameters can determine the flow behaviors and final microstructures of the products. On the other hand, the microstructure evolution during hot deformation can in turn affect the flow behaviors, and also influence the hot deformation process. Hence, it is significant to further investigate the dependence to further investigate the dependence of flow behaviors on the deformation parameters and microstructure evolution for optimizing the processing parameters[7].

In addition, it is well known that the flow behaviors of metals and alloys can be described by the constitutive models, which can be used for simulating the thermo-mechanical response of mechanical parts under the prevailing loading conditions[8]. In recent years, many constitutive models have been proposed to predict the flow stresses of metals and alloys during hot deformation, which are very critical for the accuracy of numerical simulation and the optimization of deformation parameters[9]. Considering the effects of strain on material constants, Lin et al.[10] proposed a revised hyperbolic sine constitutive equation to describe the hot deformation behaviors of 42CrMo steel. Meanwhile, Lin et al.[11] established multi-gene genetic

---

Received date: November 22, 2017
Foundation item: Fund for Doctor of Shandong Province (ZR2017BEM008, ZR2018BEE007); the Scientific Research Foundation of Shandong University of Science and Technology for Recruited Talents (2016RCJJ019, 2017RCJJ026)
Corresponding author: Zhang Hongbin, Ph. D., Lecturer, College of Mechanical and Electronic Engineering, Shandong University of Science and Technology, Qingdao 266590, P. R. China, Tel: 0086-532-8657207, E-mail: skzhanghongbin@163.com

programming, artificial neural network and Arrhenius type phenomenological models to predict the flow stress of a typical nickel-based superalloy during hot deformation. On the basis of Arrhenius-type hyperbolic sine method, Cui et al.[12] developed a constitutive model of high precision, which were ensured by the cubic piecewise functions of strain. Guo et al.[13] proposed that the hot deformation behavior of Al alloy 3003 could be described by the modified Voce type model. Furthermore, Quan et al.[14] established an artificial neural network model number to describe the complex deformation behavior of as-cast Ti-6Al-2Zr-1Mo-1V alloy[15].

On the other hand, nickel-based superalloys have been widely used in the critical parts of modern aero engine and gas turbine owing to their excellent mechanical, physical and anticorrosion properties[16]. However, there are many alloying elements in such alloys, leading to a narrow range of deformation parameters and great deformation resistance. Therefore, some investigations have been carried out to understand the effects of deformation parameters on the hot deformation behavior and microstructure evolution of nickel-based superalloys. Guo et al.[17] established the processing map of Inconel 690 alloy to optimize forming parameters, and found that the carbides assisted in DRX nucleation and restricted the coarsening of DRX grains. Wang et al.[18] found that the pre-precipitated δ phases had a great effect on the DRX process of superalloy 718. Wen et al.[19] studied the effect of deformation parameters on the DRX kinetics of a Ni-Fe-Cr-base superalloy during hot deformation. Etaati and Dehghani[20] studied the hot deformation behavior of Ni-42.5Ti-7.5Cu alloy. Although some studies have been carried out to study the hot deformation behaviors of nickel-based superalloys, the constitutive models for such alloys are still not advanced enough to account for the complex microstructure evolution. Therefore, it is very important to establish the accurate constitutive models for nickel-based superalloys, which are critical for the correct numerical simulation of hot deformation process and the reasonable optimization of deformation parameters.

In this study, the hot deformation behavior of a typical nickel-based superalloy was studied by hot compression tests in the temperature range of 1010~1160 ºC and strain rate range of 0.001~1 s^{-1}. Based on the microstructure evolution of nickel-based superalloy during hot deformation, two-stage physically-based constitutive models considering DRV and DRX mechanisms were established to describe the coupled effects of deformation temperature, strain rate, and strain on the flow behaviors of the studied alloy. In addition, the accuracy of the established constitutive models was confirmed.

1 Experiment

The studied alloy is GH99 alloy, which is a kind of nickel-based superalloy with low stacking fault energy, and it has been widely used in combustion systems, gas turbines and other related high temperature applications due to its excellent high-temperature strength, creep resistance and corrosion resistance. In addition, the γ' phase (Ni_3AlTi) is the main strengthening phase for GH99 alloy, and the highest working temperature of such alloy can reach around 1000 ºC[21]. The chemical composition (wt%) of the alloy used in this investigation is listed in Table 1.

Cylindrical specimens were machined with a diameter of 8mm and a height of 12 mm. In order to realize the homogenization of initial microstructure, the specimens were solution treated at 1100 ºC for 30 min. The microstructure of the specimens after solution treatment was observed by using an Olympus-PMG3 optical microscope, which is shown in Fig.1. It can be found that the microstructure is homogeneous, and there are some annealing twins distributed around the equiaxed grains, as indicated by the arrows.

The hot compression tests were performed using Gleeble-1500D thermomechanical simulator at four different temperatures (1010, 1060, 1110, 1160 ºC) and four different strain rates (0.001, 0.01, 0.1, 1 s^{-1}). The deformation parameters were chosen from the practice industrial hot deforming processes. The specimens were heated to the deformation temperature at a heating rate of 10 ºC/s, and held for 180 s to eliminate thermal gradient prior to the compression tests. The reduction in the height of cylinder was 50% after compression, and the specimens were immediately water quenched to preserve the high temperature microstructure. During hot compression, the load-stroke curves were converted into true stress-true strain curves by using standard equations. And then, the deformed samples were cut along the compression axis for microstructure observation. The microstructure observations were carried out by using transmission electron microscopy (TEM). In order to produce TEM foils, discs of 3 mm in diameter were punched from the tangential section slices, mechanically ground to a thickness of about 70 μm and subsequently twin-jet electropolished using with a solution of 10% perchloric acid in ethanol. The TEM examination of the deformed specimen was performed using FEI Tecnai G2 F30 transmission electron microscopy.

Table 1 Chemical composition of the alloy (wt%)

C	Cr	Ni	W	Mo	Al	Co	Ti	Fe	B	Mg	Ce	Mn	Si	P	S
0.045	18.30	Bal.	5.90	4.02	2.19	6.40	1.16	0.24	0.003	≤0.01	≤0.02	0.02	0.05	0.007	0.002

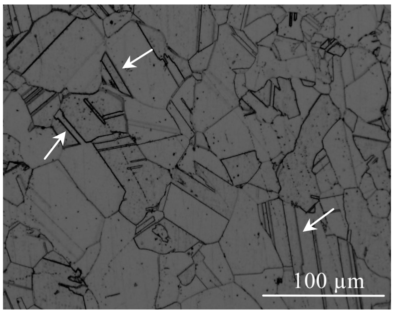

Fig.1 Optical micrograph of the alloy after solution treatment

2 Results and Discussion

2.1 True stress-true strain curves

Examples of the true stress-strain curves obtained from the hot compression of the studied superalloy are shown in Fig.2. These curves exhibit similar characteristics: there exists a peak stress at small strain due to initial work hardening, followed by a flow softening stage and then a steady stage at high strain. Such flow behaviors are consistent with the previous results for nickel-based superalloys with low stacking fault energy, indicating the occurrence of dynamic softening mechanisms during hot deformation, such as dynamic recovery (DRV) and dynamic recrystallization (DRX)[22]. In the work-hardening stage, the dislocation continually increases and rapidly accumulates, resulting in the rapid increase in flow stress[23]. In the softening stage, the effect of work hardening can be partially neutralized by the occurrence of dynamic softening mechanisms[24], which can lead to the decrease on flow stress. At the steady stage, the flow stress keeps a steady state due to the dynamic balance between the work hardening and dynamic softening.

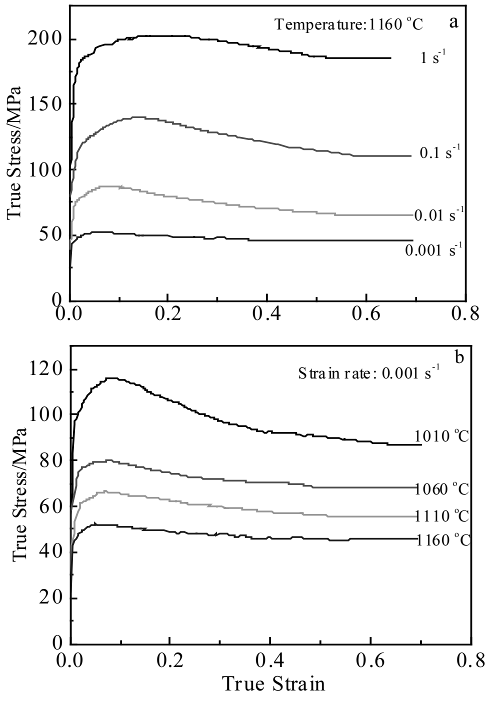

Fig.2 True stress-strain curves for the studied alloy under the tested conditions: (a) 1160 °C and (b) 0.001 s^{-1}

On the other hand, the flow stress is significantly influenced by the deformation temperature and strain rate. As shown in Fig.2a, it can be found that the flow stress increases with the decreasing deformation temperature under a given strain rate. This is because that DRV and DRX occur easily at higher deformation temperatures, which can overcome the work hardening caused by the pile-up and tangling dislocations[25]. Moreover, it is beneficial for the grain boundary mobility at the high deformation temperature[26]. Besides, it can be found that the flow stress increases with the increasing strain rate, as shown in Fig.2b. The main reason for such phenomenon is that lower strain rates can provide longer time for the nucleation and growth of DRX grains, as well as the dislocation motions (including slip, cross-slip and climb)[27, 28].

In order to confirm the occurrence of working hardening, DRV and DRX in the studied alloy during hot deformation, TEM examination was carried out. Fig.3 shows the TEM image of the alloy deformed to a true strain of 0.7 at 1160 °C with a strain rate of 1 s^{-1}. As shown in Fig.3, the DRX grains can be clearly observed, and there are almost no dislocations in the DRX grains. It can be confirmed that the occurrence of DRX rapidly eliminated the dislocations, which is consistent with the previous research[29]. The subgrain boundaries and dislocation cells can also be seen in Fig.3, which are the typical DRV structures. In addition, the dislocation networks interacted with each other to form dislocation forests and activate the work hardening[30]. Obviously, the occurrence of work hardening, DRX and DRV resulted in the complex flow behaviors of the alloy during hot deformation.

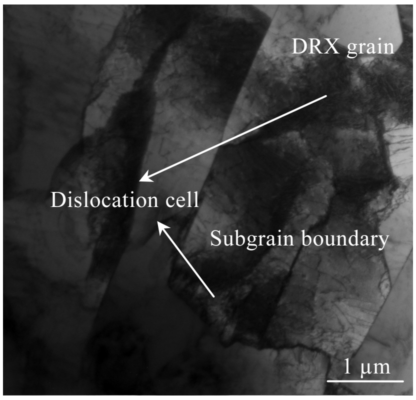

Fig.3 TEM image of the alloy deformed to a true strain of 0.7 at 1160 °C with a strain rate of 1 s^{-1}

2.2 Constitutive models of the studied alloy

2.2.1 Constitutive model during the work hardening-DRV period

In the authors' previous publication[21, 31], it has been reported that DRV and DRX are the main dynamic softening mechanisms of the studied alloy during hot deformation, which can occur simultaneously. As shown in Fig.4, the curve marked with 'DRV' assumes that DRV is the main softening mechanism and DRX is unavailable to take place. It can be found that the flow stress increases with the increasing strain, and finally reaches a saturation stress (σ_{sat}) due to the dynamic balance between the DRV and work hardening. Meanwhile, the curve marked with 'DRX' assumes that DRX is the dominant softening mechanism and DRV is weak. It can be seen that the flow stress drops gradually once the deformation degree exceeds the peak strain (ε_p), and finally reaches a steady stress (σ_{ss}) due to the dynamic balance between the work hardening and dynamic softening (including DRV and DRX). In addition, it should be noted that DRX will take place as the deformation degree exceeds the critical strain (ε_c).

Obviously, the true stress-strain curves of the studied alloy are in accord with the curve marked with 'DRX', which also includes a work-hardening stage, a softening stage and a steady stage. When the true strain is smaller than the critical strain (ε_c), DRV is the main softening mechanism and the flow stress can be calculated by the following equation[32]:

$$\sigma = \left[\sigma_{sat}^2 + \left(\sigma_0^2 - \sigma_{sat}^2\right)e^{-\Omega\varepsilon}\right]^{0.5} \quad (1)$$

where σ_0 is the yield stress, and Ω is the coefficient of DRV. In Eq.(1), there are three characteristic parameters (σ_{sat}, σ_0 and Ω) to be determined.

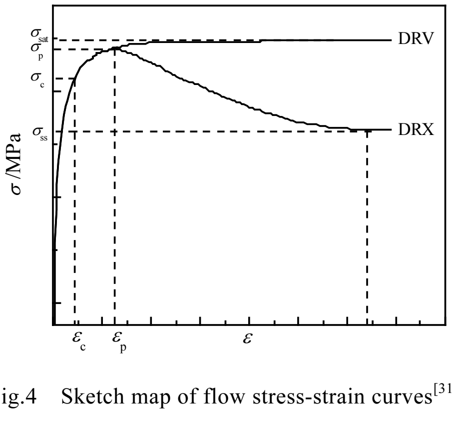

Fig.4 Sketch map of flow stress-strain curves[31]

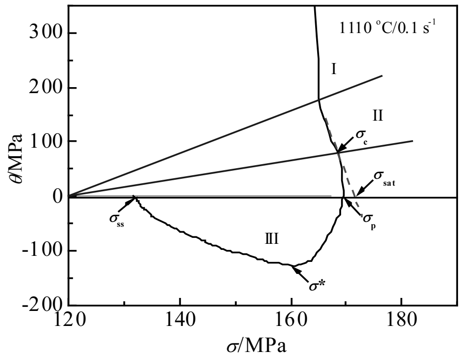

Fig.5 Relationship between the work hardening rate θ and flow stress σ under the deformation temperature of 1110 °C and strain rate of 0.1 s^{-1}

It is well known that the saturation stress (σ_{sat}) can be obtained from the work hardening rate ($d\theta = d\sigma/d\varepsilon$) versus flow stress ($\sigma$) curves, which can also reflect the microstructure evolution during hot deformation[33, 34]. The θ-σ curve of the alloy at 1110 °C and 0.1 s^{-1} is plotted on the basis of the true stress-strain curve, as shown in Fig.5. It can be found that the θ-σ curve includes three segments, and the inflection point of θ-σ curve indicates the onset of DRX in the end of segment II, which is considered as the critical stress (σ_c). Moreover, supposing DRX does not occur in the alloy, the curve will go along the red dotted line. Then, the value of θ would reduce linearly to zero and the flow stress gradually increases to the saturation stress (σ_{sat}). In addition, segment III corresponds to the deformation stage from the onset of DRX to the end of deformation. At this stage, the value of θ drops rapidly to zero when the flow stress increases to the peak stress (σ_p), and then the value of θ becomes negative owing to the softening effect of DRX. When the θ value reaches the negative peak, the flow stress for the maximum softening rate (σ^*) can be determined[35]. As a new dynamic balance between the work hardening and dynamic softening induced by DRX and DRV is reached, the value of θ will increase to zero again and the flow stress will reach the steady stress (σ_{ss}). By using θ-σ curves, the values of σ_{sat} under different deformation conditions can be obtained. Moreover, the combined effects of deformation temperature and strain rate on the flow stress of alloys can be characterized by Zener-Hollomon parameter (Z), which is expressed as[36],

$$Z = \dot{\varepsilon}\exp(Q/RT) \quad (2)$$

where $\dot{\varepsilon}$ is the strain rate (s^{-1}). R is the gas constant. T is the absolute temperature (K). Q is activation energy of the alloy during hot deformation (J/mol), which has been calculated to be 427 626 J/mol in authors' previous publications[21].

Fig.6 shows the relationship between lnσ_{sat} and ln$Z$. According to the slope and intercept of the fitting line, σ_{sat} can be expressed as,

$$\sigma_{sat} = 0.24252Z^{0.18726} \quad (3)$$

Furthermore, the yield stress (σ_0) at various deformation temperatures and strain rates can be directly obtained from the true stress-strain curves. Meanwhile, the values of σ_0

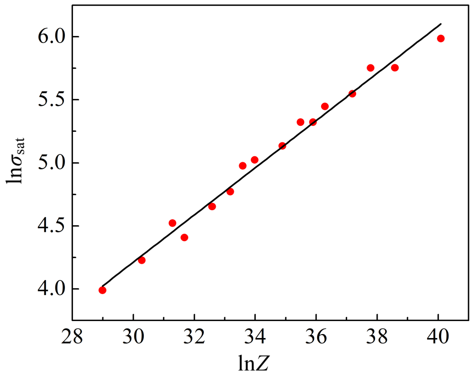

Fig.6 Relationship between $\ln\sigma_{sat}$ and $\ln Z$

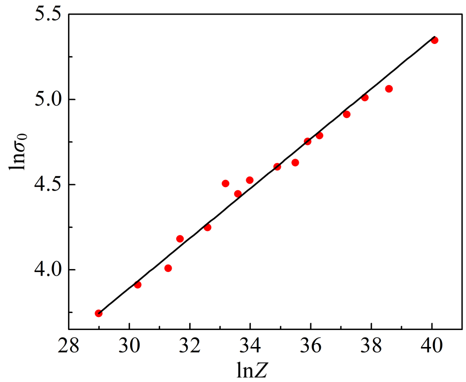

Fig.7 Relationship between $\ln\sigma_0$ and $\ln Z$

can be also expressed as the function of Zener-Hollomon parameter (Z). Fig.7 shows the relationship between $\ln\sigma_0$ and $\ln Z$, and σ_0 can be expressed as,

$$\sigma_0 = 0.60891Z^{0.14629} \tag{4}$$

It should be noted that DRV is the main softening mechanism when the true strain is smaller than the critical strain[37]. Therefore, the value of Ω can be calculated on the basis of the true stress-strain curve before critical strain. Taking logarithm on both sides of Eq.(1), then Eq.(1) can be written as:

$$\Omega\varepsilon = \ln\left(\frac{\sigma_{sat}^2 - \sigma_0^2}{\sigma_{sat}^2 - \sigma^2}\right) \tag{5}$$

The relationship between $\ln[(\sigma_{sat}^2-\sigma_0^2)/(\sigma_{sat}^2-\sigma^2)]$ and ε under the deformation temperature of 1160ºC and strain rate of 0.01 s^{-1} is shown in Fig.8. The value of Ω can be determined by the linear regression method. Based on the above method, the values of Ω can be determined for the different tested conditions. Fig.9 shows the relationship between $\ln\Omega$ and $\ln Z$, and Ω can be expressed as:

$$\Omega = 6884.79062Z^{-0.17238} \tag{6}$$

Therefore, the constitutive models during the work hardening-dynamic recovery period of the studied alloy can be summarized as:

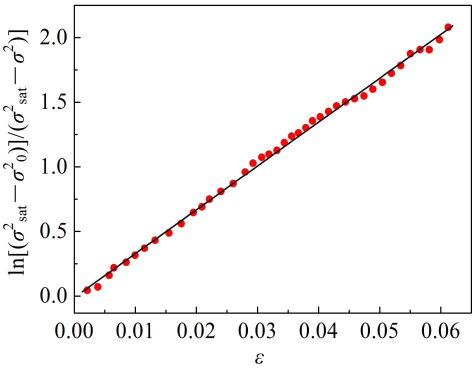

Fig.8 Relationship between $\ln[(\sigma_{sat}^2 - \sigma_0^2)/(\sigma_{sat}^2 - \sigma^2)]$ and ε

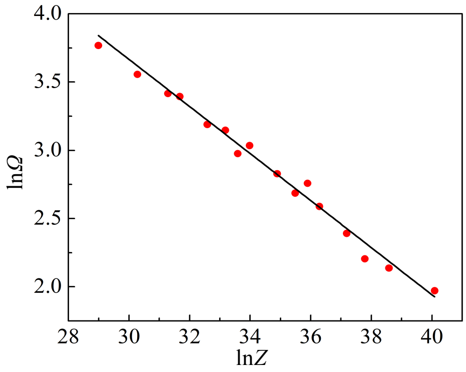

Fig.9 Relationship between $\ln\Omega$ and $\ln Z$

$$\begin{cases} \sigma = \left[\sigma_{sat}^2 + \left(\sigma_0^2 - \sigma_{sat}^2\right)e^{-\Omega\varepsilon}\right]^{0.5} \\ \sigma_{sat} = 0.24252Z^{0.18726} \quad \sigma_0 = 0.60891Z^{0.14629} \\ \Omega = 6884.79062Z^{-0.17238} \\ Z = \dot{\varepsilon}\exp(427626/RT) \end{cases} \tag{7}$$

2.2.2 Constitutive model during the DRX period

The onset of DRX depends on the density of dislocations. Once the dislocations of deformed alloy increase and accumulate to an extent during hot deformation, the nucleation and growth of DRX grains will take place near the grain boundaries. In other words, DRX nucleus would form at grain boundaries as the deformation degree is larger than the critical strain (ε_c). In addition, at high temperatures and low strain rates, the occurrence of DRX becomes more and more obvious[26]. The volume fraction of DRX (X_{drx}) can be predicted by the modified Avrami-type equation[38]:

$$X_{drx} = 1 - \exp\left[-k\left(\frac{\varepsilon - \varepsilon_c}{\varepsilon^*}\right)^n\right] \quad (\varepsilon \geqslant \varepsilon_c) \tag{8}$$

where ε^* is the strain for maximum softening rate; ε_c is the critical strain; k and n are material constants. Meanwhile, the flow stress of materials featured by DRX can also be expressed as[26]:

$$X_{\mathrm{drx}}=\frac{\sigma_{\mathrm{rec}}-\sigma}{\sigma_{\mathrm{sat}}-\sigma_{\mathrm{ss}}}\quad(\varepsilon\geqslant\varepsilon_{\mathrm{c}})\tag{9}$$

where σ_{rec} is the flow stress when DRV is the main softening mechanism, which can be calculated by Eq.(1). Taking Eq.(8) into Eq.(9), the flow stress (σ) during the DRX period can be expressed as:

$$\sigma=\sigma_{\mathrm{rec}}-(\sigma_{\mathrm{sat}}-\sigma_{\mathrm{ss}})\left\{1-\exp\left[-k\left(\frac{\varepsilon-\varepsilon_{\mathrm{c}}}{\varepsilon^{*}}\right)^{n}\right]\right\}\quad(\varepsilon\geqslant\varepsilon_{\mathrm{c}})\tag{10}$$

In Eq.(10), there are five characteristic parameters (σ_{ss}, ε_{c}, ε^*, k and n) to be determined. The steady stress (σ_{ss}) can be obtained from the θ-σ curve. Fig.10 shows the relationship between lnσ_{ss} and ln$Z$, and σ_{ss} can be expressed as,

$$\sigma_{\mathrm{ss}}=0.13190Z^{0.19832}\tag{11}$$

As mentioned in section 2.2.1, the flow stress for the maximum softening rate (σ^*) and critical stress (σ_{c}) can also be obtained from the θ-σ curve. And then, ε^* and ε_{c} can be determined from the true stress-strain curves, which are listed in Table 2. It can be found that the values of ε_c decrease with the increase of deformation temperature, indicating that the DRX behavior occurs easily at the higher deformation temperature. Such phenomenon is related to the lower driving force and higher mobility of grain boundaries at the higher deformation temperature[39]. On the other hand, the values of ε_c decrease with the decrease of strain rate, indicating that the DRX behavior occurs easily at the lower strain rate. This is because that there is enough time for energy accumulation to reduce the driving force under the lower strain rate[40].

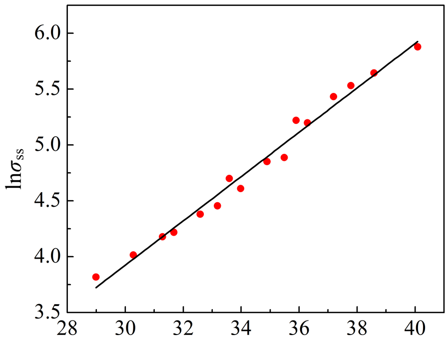

Fig.10 Relationship between lnσ_{ss} and ln$Z$

Table 2 Values of ε^* and ε_{c}

Parameter	Strain rate, $\dot{\varepsilon}$ /s^{-1}	1010 °C	1060 °C	1110 °C	1160 °C
ε^*	1	0.332	0.301	0.265	0.242
	0.1	0.269	0.258	0.231	0.212
	0.01	0.243	0.220	0.202	0.174
	0.001	0.210	0.184	0.169	0.158
ε_{c}	1	0.125	0.110	0.106	0.098
	0.1	0.105	0.101	0.088	0.085
	0.01	0.090	0.080	0.070	0.062
	0.001	0.074	0.059	0.055	0.052

Fig.11 shows the relationship between lnε_{c} and ln$Z$, and ε_{c} can be expressed as:

$$\varepsilon_{\mathrm{c}}=0.00454Z^{0.08397}\tag{12}$$

In addition, the value of ε^* can also be represented as a power function of Zener-Hollomon parameter. Fig.12 shows the relationship between lnε^* and ln$Z$, and ε^* can be expressed as,

$$\varepsilon^*=0.02290Z^{0.06591}\tag{13}$$

Taking logarithm on both sides of Eq.(8), Eq.(8) can be written as:

$$\ln[-\ln(1-X_{\mathrm{drx}})]=\ln k+n\ln\left(\frac{\varepsilon-\varepsilon_{\mathrm{c}}}{\varepsilon^{*}}\right)\tag{14}$$

In Eq.(14), X_{drx} can be calculated by Eq.(9). The values of n and k can be determined by the linear regression method. Fig.13 shows the relationship between $\ln[-\ln(1-X_{\mathrm{drx}})]$ and $\ln(\varepsilon-\varepsilon_{\mathrm{c}}/\varepsilon^*)$ for the alloy deformed at 1160 °C and 0.01 s^{-1}. On the basis of the slope and intercept of the fitting line, the values of n and k can be obtained. By applying the above method, the values of n and k under different conditions are determined and listed in Table 3.

It is notable that the values of n are dependent on the deformation temperature and strain rate. The relationship between n and Zener-Hollomon parameter is illustrated in Fig.14, and n can be represented as a power function of Zener-Hollomon parameter:

$$n=0.03272Z^{0.10897}\tag{15}$$

On the other hand, from Table 3 it can be found that the values of k are independent of the deformation temperature and strain rate. The values of k are calculated in the range of 0.777~0.927, and its average value can be evaluated as 0.855.

Hence, the constitutive model during DRX period ($\varepsilon\geqslant\varepsilon_c$) can be expressed as:

$$\begin{cases}\sigma=\sigma_{\mathrm{rec}}-(\sigma_{\mathrm{sat}}-\sigma_{\mathrm{ss}})\left\{1-\exp\left[-k\left(\frac{\varepsilon-\varepsilon_{\mathrm{c}}}{\varepsilon^{*}}\right)^{n}\right]\right\}(\varepsilon\geqslant\varepsilon_{\mathrm{c}})\\ \sigma_{\mathrm{ss}}=0.13190Z^{0.19832}\\ \varepsilon_{\mathrm{c}}=0.00454Z^{0.08397}\quad\varepsilon^*=0.02290Z^{0.06591}\\ n=0.03272Z^{0.10897}\quad k=0.855\end{cases}\tag{16}$$

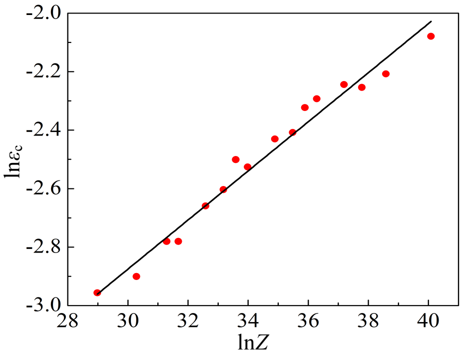

Fig.11 Relationship between lnε_{c} and ln$Z$

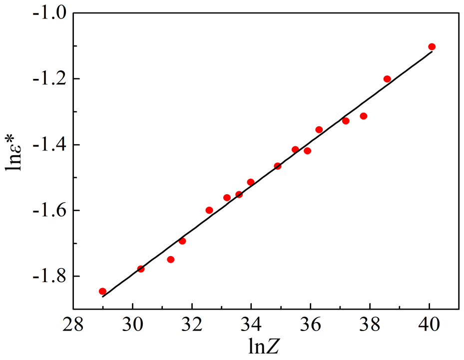

Fig.12 Relationship between $\ln\varepsilon^*$ and $\ln Z$

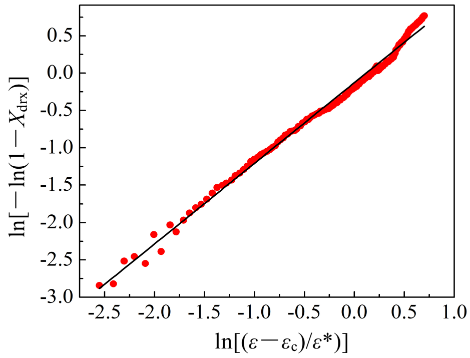

Fig.13 Relationship between $\ln[-\ln(1-X_{drx})]$ and $\ln[(\varepsilon-\varepsilon_c)/\varepsilon^*]$ for the alloy deformed at 1160 °C and 0.01 s^{-1}

Table 3 Values of k and n

Parameter	Strain rate, $\dot{\varepsilon}$ /s^{-1}	1010 °C	1060 °C	1110 °C	1160 °C
k	1	0.915	0.893	0.927	0.910
	0.1	0.811	0.780	0.811	0.791
	0.01	0.800	0.874	0.777	0.887
	0.001	0.844	0.876	0.881	0.902
n	1	2.450	2.200	1.857	1.590
	0.1	2.102	1.886	1.481	1.338
	0.01	1.521	1.314	1.129	1.025
	0.001	1.163	1.027	0.892	0.781

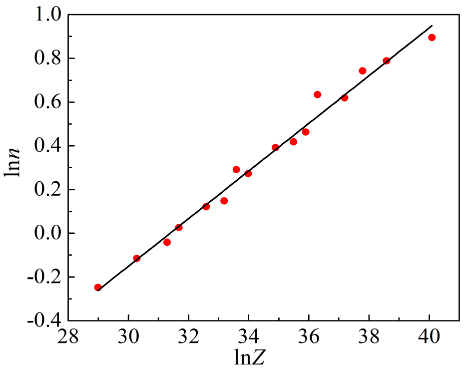

Fig.14 Relationship between $\ln n$ and $\ln Z$

2.2.3 Verification of the developed constitutive models

In order to verify the precision of the developed constitutive models, comparison of the measured and predicted flow stresses was carried out. Fig.15 shows the comparisons between the predicted and measured true stress-strain curves of the alloy deformed under different conditions. Obviously, it can be found that the predicted flow stresses correlate well with the measured flow stresses.

In order to further evaluate the accuracy of the developed constitutive models, the correlation coefficient (R) and average absolute relative error (AARE) between the predicted and measured flow stress were also calculated. The correlation coefficient is commonly used to represent the strength of linear relationship between experimental values and predicted values, which can be expressed as[41]:

$$R=\frac{\sum_{i=1}^{N}(E_i-\overline{E})(P_i-\overline{P})}{\sqrt{\sum_{i=1}^{N}(E_i-\overline{E})^2\sum_{i=1}^{N}(P_i-\overline{P})^2}} \tag{17}$$

where E_i is the experimental value, P_i is the predicted value, $\overline{E}$ and $\overline{P}$ are the mean values of E_i and P_i, respectively, N is the number of experiment samples. In addition, the average absolute relative error is an unbiased statistical parameter for determining the predictability of the equation, which can be expressed as[41]:

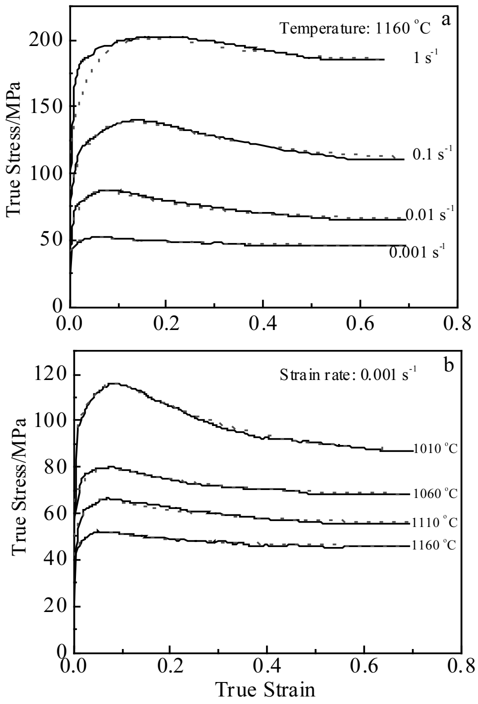

Fig.15 Comparison of the predicted and measured true stress-strain curves of the alloy under the tested conditions: (a) 1160 °C and (b) 0.001 s^{-1}

$$\mathrm{AARE}=\frac{1}{N}\sum_{i=1}^{N}\left|\frac{E_i-P_i}{E_i}\right|\times 100\% \qquad (18)$$

Fig.16 shows correlation between the predicted and measured flow stresses of the alloy deformed under different conditions. The values of R are 0.995 50 and 0.999 06, indicating a good correlation between the predicted and measured flow stresses. Meanwhile, the values of AARE are 2.19% and 0.8%, implying the good prediction capability of the developed constitutive models.

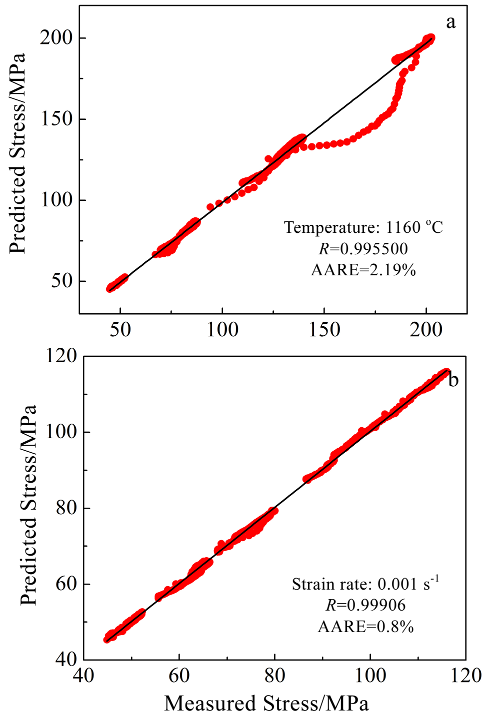

Fig.16 Correlation between the predicted and measured flow stresses of the alloy under the tested conditions: (a) 1160 ºC and (b) 0.001 s^{-1}

3 Conclusions

1) Hot deformation behaviors of a typical nickel-based superalloy were studied by hot compression tests in the temperature range of 1010~1160 ºC and strain rate range of 0.001~1 s^{-1}. The results reveal that the flow stress increases with the decrease in deformation temperature or the increase in strain rate.

2) Based on the experimental data, the constitutive models were established to predict the flow stresses during the work hardening-dynamic recovery (DRV) and dynamic recrystallization (DRX) periods. In particular, the modified DRX kinetic equation was used to develop the constitutive models in DRX period.

3) Comparisons between the measured and predicted flow stresses were carried out, while the correlation coefficient and average absolute relative error were calculated, which confirms the accuracy and good prediction capability of the developed constitutive models.

References

1 Chen J Y, Dong J X, Zhang M C *et al. Materials Science & Engineering A*[J], 2016, 673: 122
2 Lin Y C, Wu F, Wang Q W *et al. Vacuum*[J], 2018, 151: 283
3 Saravanan L, Senthilvelan T. *Transactions of the Indian Institute of Metals*[J], 2016, 69(10): 1
4 Belbasi M, Salehi M T, Mousavi S A A A *et al. Materials Science and Engineering A*[J], 2013, 560: 96
5 Tan L M, Huang Z, Liu F *et al. Materials & Design*[J], 2017, 131: 60
6 Momeni A, Dehghani K, Ebrahimi G R *et al. Metallurgical and Materials Transactions A*[J], 2013, 44(12): 5567
7 Mandal S, Bhaduri A, Sarma V S. *Metallurgical and Materials Transactions A*[J], 2012, 43(6): 2056
8 Lin Y C, Dong W Y, Zhou M *et al. Materials Science and Engineering A*[J], 2018, 718: 165
9 Duc-Toan N, Seung-Han Y, Dong-Won J *et al. The International Journal of Advanced Manufacturing Technology*[J], 2012, 62(5-8): 551
10 Lin Y C, Chen M S, Zhong J. *Computational Materials Science*[J], 2008, 42(3): 470
11 Lin Y C, Nong F Q, Chen X M *et al. Vacuum*[J], 2017, 137: 104
12 Cui J H, Yang H, Sun Z C *et al. Rare Metal Materials and Engineering*[J], 2012, 41(3): 397
13 Guo J H, Zhao S D, Murakami R *et al. Journal of Alloys and Compounds*[J], 2013, 566: 62
14 Quan G Z, Mao A, Luo G C *et al. Materials & Design*[J], 2013, 52(24): 98
15 Xiao X, Liu G Q, Hu B F *et al. Computational Materials Science*[J], 2012, 62: 227
16 Zhang H B, Zhou H P, Qin S X *et al. Materials Science & Engineering A*[J], 2017, 696: 290
17 Guo S L, Li D F, Pen H J *et al. Journal of Nuclear Materials*[J], 2011, 410(1): 52
18 Wang Y, Zhen L, Shao W Z *et al. Journal of Alloys and Compounds*[J], 2009, 474(1): 341
19 Wen D X, Lin Y C, Zhou Y. *Vacuum*[J], 2017, 141: 316
20 Etaati A, Dehghani K. *Materials Chemistry and Physics*[J], 2013, 140(1): 208
21 Zhang H B, Zhang K F, Lu Z *et al. Materials Science and Engineering A*[J], 2014, 604: 1
22 Guo Q, Li D F, Guo S L. *Materials and Manufacturing Processes*[J], 2012, 27(9): 990
23 Cai D Y, Xiong L Y, Liu W C *et al. Materials Characterization* [J], 2007, 58(10): 941
24 Li J, Wang H M. *Materials Science and Engineering A*[J],

2010, 527(18): 4823

25 Chen F, Cui Z S, Chen S J. *Materials Science and Engineering A*[J], 2011, 528(15): 5073

26 Lin Y C, Chen X M, Wen D X *et al. Computational Materials Science*[J], 2014, 83: 282

27 Momeni A, Dehghani K. *Metals and Materials International*[J], 2010, 16(5): 843

28 Zhang H B, Zhang K F, Zhou H P *et al. Materials & Design*[J], 2015, 80: 51

29 Zong Y Y, Shan D B, Lü Y *et al. International Journal of Hydrogen Energy*[J], 2007, 32(16): 3936

30 Habibnejad-Korayem M, Mahmudi R, Poole W J. *Materials Science & Engineering A*[J], 2013, 567: 89

31 Zhang H B, Zhang K F, Jiang S S *et al. Journal of Materials Research*[J], 2015, 30(7): 1029

32 Liu Y G, Li M Q, Luo J. *Materials Science and Engineering A* [J], 2013, 574: 1

33 Mirzadeh H, Najafizadeh A. *Materials & Design*[J], 2010, 31(3): 1174

34 Yanagida A, Yanagimoto J. *Journal of Materials Processing Technology*[J], 2004, 151(1): 33

35 Jia J B, Zhang K F, Lu Z. *Materials Science and Engineering A*[J], 2014, 607: 630

36 Balasubrahmanyam V, Prasad Y. *Materials Science and Engineering A*[J], 2002, 336(1): 150

37 Chen X M, Lin Y C, Wen D X *et al. Materials & Design*[J], 2014, 57: 568

38 Lv B J, Peng J, Shi D W *et al. Materials Science and Engineering A*[J], 2013, 560: 727

39 Imbert C A C, McQueen H J. *Materials Science and Engineering A*[J], 2001, 313(1-2): 104

40 Ning Y Q, Fu M W, Chen X. *Materials Science and Engineering A*[J], 2012, 540: 164

41 Quan G Z, Lv W Q, Mao Y P *et al. Materials & Design*[J], 2013, 50: 51

基于动态再结晶动力学方程的镍基高温合金热变形流变应力预测

周海萍[1]，张弘斌[1]，刘　杰[1]，秦升学[1,2]，吕玉廷[1]

(1. 山东科技大学，山东 青岛 266590)

(2. 青岛 RTP 工程技术中心，山东 青岛 266590)

摘　要：采用等温热压缩实验，研究了 1 种典型镍基高温合金在 1010~1160 ℃及 0.001~1 s^{-1} 条件下的高温流变行为。结果表明，在合金的高温变形过程中发生了动态回复(DRV)以及动态再结晶(DRX)现象。通过深入分析不同变形条件下合金的高温流变行为，分别建立了合金在加工硬化-动态回复阶段以及动态再结晶阶段的流变应力本构方程。其中，在动态再结晶阶段，流变应力本构方程的建立是基于一种新型的动态再结晶动力学方程，该方程中引入了最大软化速率应变。此外，采用线性拟合的方法，建立了本构方程中材料常数与 Zener-Hollomon 参数间的函数关系。同时，通过对比分析流变应力的实测值和预测值，并计算两者之间的相关系数(R)和平均相对误差绝对值(AARE)，验证了所建立本构方程的准确性，它可以精确预测所研究合金的高温流变应力。

关键词：镍基高温合金；本构方程；加工硬化；动态回复；动态再结晶

作者简介：周海萍，女，1987 年生，博士，讲师，山东科技大学机械电子工程学院，山东 青岛 266590，电话：0532-86057207，E-mail: zhouhp325@163.com